Assessment of Hydrocarbon Production Induced Surface Deformation over Inglewood oilfield, Los Angeles

Imeime Uyo[1], Mahdi Motagh[2,1], Mahmud H. Haghighi[1] Vamshi Karanam[3]

[1] *Institute of Photogrammetry and Geoinformation, Leibniz University Hannover, Germany*
[2] *GFZ Helmholtz Centre for Geosciences, Potsdam, Germany*
[3] *Southern Methodist University, Texas, United States of America.*

Keywords: InSAR, Ground deformation, Inglewood Oil Field, SBAS, MintPy, HyP3.

Abstract

This study investigates surface deformation in the Inglewood oilfield using Sentinel-1 InSAR time-series analysis and its relationship with reservoir fluid dynamics. A total of 491 SAR images acquired between January 2020 and October 2025 were processed to derive line-of-sight (LOS) deformation from ascending and descending geometries. The results reveal a low-magnitude deformation field (< ±2 cm/year) characterized by localized subsidence–uplift patterns associated with hydrocarbon production. Decomposition of LOS measurements indicate predominantly vertical motion, with uplift and subsidence rates of up to +0.8 cm/year and −1.6 cm/year, respectively, while horizontal displacements remain minor (≤ ±1.0 cm/year).

To assess spatial variability, the study area was subdivided into three localized high-deformation zones, within which the relationship between reservoir fluid balance and surface deformation was evaluated. The results show that deformation is closely linked to fluid balance, although the strength of this relationship varies between zones. In Zone 3, a strong correlation ($r \approx 0.75$) is observed between cumulative net fluid balance and uplift. Zone 1 exhibits a delayed response, with peak correlation ($r \approx 0.88$) at a lag of approximately 5–6 months. In contrast, Zone 2 shows weaker coupling ($r \approx 0.42$) despite exhibiting the highest subsidence, suggesting the influence of geological heterogeneity, structural controls, and additional wells not included in the analysis. These findings demonstrate the capability of InSAR to detect subtle deformation and provide valuable insights into reservoir processes.

1. Introduction

Surface deformation in oil and gas reservoirs can result in significant costs, including well failures, damage to surface infrastructure, and in some cases the triggering of regional seismicity (Fokker et al., 2018; Geertsma, 1973). Therefore, regular monitoring and modeling of ground movement has become critical for proper evaluation and mitigation of hazards associated with oilfield operations.

In contrast to the large and rapid ground movements typically produced by earthquakes, coal extraction, or volcanic activity, the surface deformation linked to hydrocarbon production develops slowly and occurs at a much lower rate (Xu et al., 2023). Because the resulting deformation represents the response of the reservoir to dynamic pressure variations, where volumetric expansion or contraction occurs, it generally conforms to predictable volumetric strain patterns. This deformation typically manifests as a broad, bowl-shaped subsidence feature, characterized by vertical ground displacement accompanied by lateral movement toward the zone of maximum pressure reduction (Rocca et al., 2013; Tamburini et al., 2010).

Conventional ground-based methods such as levelling and total stations yield precise measurements but are labour- and time-intensive. GPS monitoring, while useful, requires the deployment of stations and provides relatively coarse spatial coverage. In contrast, satellite Interferometric Synthetic Aperture Radar (InSAR) can estimate surface deformation across broad areas with high spatial and temporal resolution (Lu and Dzurisin, 2014). It is highly effective for monitoring oil field regions, facilitating the detection and quantitative assessment of ground surface deformations and associated geomechanical responses induced by reservoir pressure variations (Fielding et al., 1998; Ringrose et al., 2013). InSAR-based monitoring improves reservoir characterization and provides more reliable estimates of subsurface parameters. (Elliott et al., 2016; Staniewicz et al., 2020).

InSAR has been effectively applied to monitor hydrocarbon-production induced surface deformation in several regions, including the Permian Basin (Karanam & Lu, 2023; Staniewicz et al., 2020), the Groningen gas field, the Netherlands (Ketelaar, 2009), Yellow River Delta, China (Liu et al., 2016), Karamay oilfield, China (Xu et al., 2023; Yang et al., 2019), Tengiz oilfield, Kazakhstan (Grebby et al., 2019).

Shi et al. (2022) presented a multi-track SBAS-based InSAR framework to derive long-term vertical deformation in the Lost Hills oilfield using ERS, Radarsat-1, and Envisat datasets. Their results revealed significant spatial variability, with uplift rates up to 20 mm/year and subsidence reaching −90 mm/year. By integrating InSAR-derived deformation with injection and production data through multivariate polynomial regression, they demonstrated that subsidence exhibits a linear relationship with fluid extraction, whereas uplift follows a nonlinear behavior. These findings highlight the complexity of reservoir deformation processes and the importance of integrating geodetic and operational datasets for accurate interpretation.

The Inglewood Oil Field is situated in the northeastern part of the Los Angeles Basin, California, at the northern end of the prolific Newport–Inglewood fault trend. Discovered in 1924, it is among the largest and most productive urban oil fields in the United States, covering approximately 1,000 acres. The study area is shown in Figure 1.

Exploration and development began in the early 20th century, with the first commercial production initiated by the Standard Oil Company of California. Over its operational history, more than

This contribution has been peer-reviewed. The double-blind peer-review was conducted on the basis of the full paper.
https://doi.org/10.5194/isprs-annals-XI-3-2026-485-2026 | © Author(s) 2026. CC BY 4.0 License.

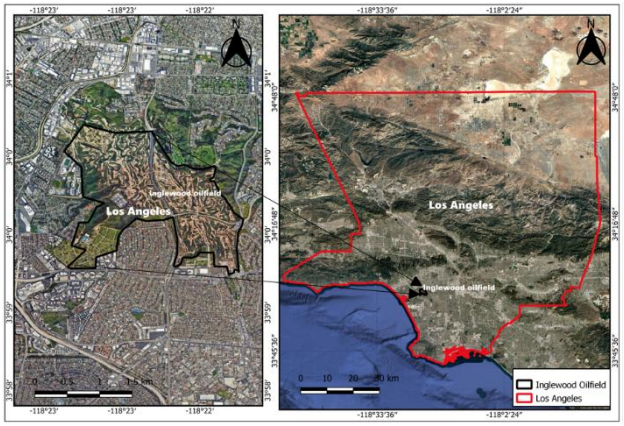

Figure 1. Study area map

1,600 wells have been completed, resulting in an estimated ultimate recovery of approximately 400 million barrels of oil from a productive area of about 1,215 acres.

At present, the Inglewood Oil Field remains one of the most productive fields in the Los Angeles Basin, with annual production averaging between 2.5 and 3.1 million barrels over the past decade.

The urban setting of the Inglewood oilfield makes it a distinctive hydrocarbon production site. Surrounded by densely populated communities, the field is embedded within areas used for residential, commercial, and recreational purposes. This juxtaposition of large-scale petroleum production and metropolitan development underscores both the economic significance of the field and the environmental and social sensitivities associated with its operation (Wright, 1987).

Urban hydrocarbon fields are generally associated with numerous problems including surface deformation. Monitoring the deformation rate in the Inglewood oilfield is of critical importance due to its urban setting and history of deformation-related hazards. The 1963 Baldwin Hills Dam (within the Inglewood oilfield) failure serves as a stark reminder of the potential risks associated with unmonitored ground movement linked to oilfield activities. Subsequent investigations revealed that differential subsidence, correlated with hydrocarbon production, contributed to structural instability and catastrophic failure (Castle & Yerkes, 1976; Chilingar & Endres, 2005). Given the proximity of the Inglewood oilfield to densely populated areas and vital infrastructure, continuous and precise monitoring of surface deformation is essential to ensure public safety, guide sustainable urban development, and mitigate geotechnical and environmental risks associated with ongoing reservoir operations.

Ground deformation in the Inglewood oilfield, has been monitored since 2010 under the Accumulated Ground Movement Study (AGMS), which transitioned from ground surveys to InSAR-based monitoring for improved spatial resolution. Monitoring continued until 2024, providing valuable insights into surface deformation linked to oilfield operations (Walker, 2025). Given the oilfield’s urban setting and history, continued observation is essential for assessing its stability and mitigating potential risks

The aim of this study is to investigate the relationship between reservoir fluid dynamics and surface deformation by integrating InSAR-derived vertical displacement measurements with well-based injection and production data. Specifically, the study seeks to assess how variations in fluid balance influence ground deformation within localized high-deformation zones.

By integrating multi-year InSAR observations with active injection and production well data, this study evaluates ground deformation patterns and assesses subsurface stability. It further investigates the relationship between surface deformation and reservoir fluid processes, with particular emphasis on the effects of fluid injection and withdrawal.

2. Data and Methods

2.1 InSAR data preparation

Our dataset comprises 491 Sentinel-1 SAR images acquired between January 2020 and October 2025 from both ascending and descending acquisition geometries (ascending track 240; descending track 251). Image coregistration and the generation of differential single-master interferograms were performed using the GAMMA SAR software (Wegnüller et al., 2016). Subsequent time-series analysis was carried out using the SARvey software, an open-source InSAR framework designed for local-scale displacement detection (Piter et al., 2025).

The workflow begins with a stack of co-registered single-look complex (SLC) images generated in GAMMA, which are ingested and subsetted to the specified time span according to the study period.

An interferometric network is constructed based on temporal and perpendicular baseline constraints, following the Small Baseline Subset (SBAS) approach (Berardino et al., 2003). The interferometric network and temporal baseline for the Sentinel-1 datasets are shown in Figure 3.

The phase quality of each pixel is evaluated through the estimation of temporal phase coherence (Zhao & Mallorqui, 2019), which serves as a criterion for point selection.

A subset of highly coherent pixels, referred to as first-order points, is initially identified. These points exhibit stable phase behavior and are used to estimate the atmospheric phase screen (APS). After removing potential outliers from this network of first-order points, phase unwrapping is performed in both temporal and spatial domains (Bioucas-Dias & Valadao, 2007; Boykov & Kolmogorov, 2004). The displacement time series is retrieved by inverting the interferogram network. In a subsequent step, a denser set of second-order points is selected based on a temporal coherence threshold (≥ 0.7). The APS estimated from the first-order points is removed from these additional pixels. Phase unwrapping is then performed jointly by linking second-order points to the established first-order network, followed by inversion of the interferometric network to obtain displacement timeseries.

Finally, the APS is refined by re-estimating it from the displacement time series of the first-order points and interpolating it to the locations of second-order points. The combined set of first- and second-order points provides a densified spatial sampling of surface deformation, with displacement time series derived through joint phase unwrapping and network inversion. The methodological workflow is illustrated in Figure 2.

This contribution has been peer-reviewed. The double-blind peer-review was conducted on the basis of the full paper.
https://doi.org/10.5194/isprs-annals-XI-3-2026-485-2026 | © Author(s) 2026. CC BY 4.0 License.

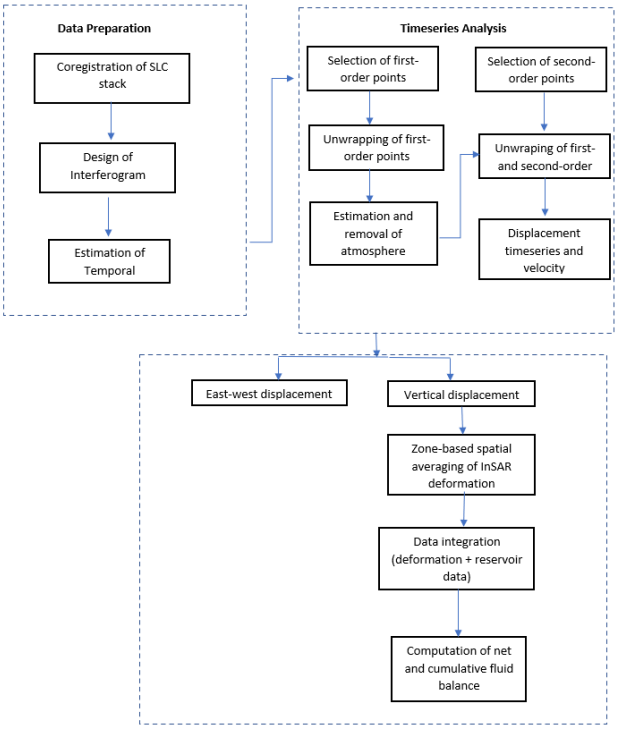

Figure 2. Methodological workflow

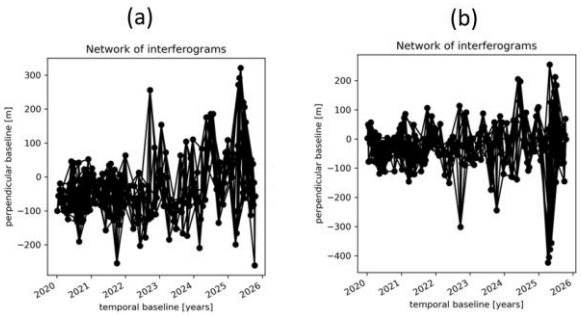

Figure 3. Interferometric network of Sentinel-1 data, showing perpendicular baseline versus temporal baseline for (a) ascending and (b) descending tracks.

2.2 Decomposition of Velocities

To derive the horizontal and vertical components of ground deformation from InSAR, the ascending and descending line-of-sight (LOS) velocity fields were combined. This method projects the LOS displacements from the two viewing geometries into horizontal and vertical directions based on the satellite incidence and azimuth angles.

This study used 2 sets of InSAR observations, for a single set of SAR data, the line of sight (LOS) velocity (V_{los}) that was derived for each pixel by applying the SBAS method can be express as:

$$V_{los} = V_V \cos\theta - (V_e \cos\alpha - V_n \sin\alpha)\sin\theta \quad (1)$$

where α is the azimuth of the LOS vector, θ is the incident angle and V_n, V_V are the velocities in east-west, north-south and vertical directions, respectively. The north-south direction is least sensitive to displacement because of the near-polar orbits of the spaceborne SAR systems. By excluding this component, equation (1) transforms into the following form.

$$V_{los} = V_V \cos\theta - V_e \cos\alpha \sin\theta \quad (2)$$

$$\begin{pmatrix} V_{los}^a \\ V_{los}^d \end{pmatrix} = \begin{pmatrix} \cos\theta^a & -\cos\alpha^a \sin\theta^a \\ \cos\theta^d & -\cos\alpha^d \sin\theta^d \end{pmatrix} \begin{pmatrix} V_v \\ V_e \end{pmatrix} \quad (3)$$

where the subscripts a and d refer to ascending and descending geometries, respectively. Since the SAR sensors used for the study cover different time periods, resulting in in different temporal sampling of ground motion, Eq. (3) is applied to the velocity maps which cover the same time periods and have the same spatial resolution (Motagh et al., 2017; Samsonov & d’Oreye, 2012)

Decomposition of velocities is essential in oil-field deformation studies because surface movement caused by hydrocarbon extraction typically involves a combination of vertical subsidence from reservoir compaction and horizontal displacement driven by lateral stress redistribution (Tang et al., 2024).

2.3 Integration of InSAR with Hydrocarbon Exploration History

Monthly injection and production data were obtained from the California Department of Conservation, Geologic Energy Management Division (CalGEM) WellSTAR public database (https://wellstar-public.conservation.ca.gov/).

The dataset comprises well-level operational records for both water injection (waterflooding) and hydrocarbon production. Injection data consist of monthly water or steam injection volumes reported in barrels (bbl), while production data include oil (bbl), gas (Mcf), and produced water (bbl).

For consistency in volumetric analysis, total liquid production was calculated as the sum of oil and produced water volumes, both expressed in barrels.

The raw datasets were downloaded portable document format (PDF) files and subjected to pre-processing, including column standardization, date parsing, unit harmonization, and removal of invalid or missing entries. Monthly time series were then constructed for each well based on the reporting period.

A subset of injection and production wells was selected based on their spatial proximity to localized high-deformation zones identified from the InSAR-derived displacement field. These zones correspond to areas exhibiting the largest magnitudes of surface deformation (both subsidence and uplift) within the broader study area. Wells located within or immediately adjacent to these zones were chosen to ensure that the analysis focuses on locations where reservoir processes are most likely to influence observed surface deformation.

Table 1. Summary of well datasets used for analysis, including well type, temporal coverage, and record count.

Well name	Well Type	Time Range	Number of Records
BC 641	Injection	1997-2026	360
LAI-VIC-LW 4	Injection	1977 -2026	601
Stocker 39	Injection	1977-2026	743
VRU 609	Injection	2006-2026	241
VRU 134	Injection	1977-2026	602
Vickers 1 104	Injection	1977-2026	786
BC 642	Production	1997-2026	345
LAI 1 945	Production	2005-2026	248
LAI 1 146	Production	1977-2026	589

This contribution has been peer-reviewed. The double-blind peer-review was conducted on the basis of the full paper.
https://doi.org/10.5194/isprs-annals-XI-3-2026-485-2026 | © Author(s) 2026. CC BY 4.0 License.

Stocker 36	Production	1977-2026	589
VRU 708	Production	2006-2026	241
VRU_275	Production	1997-2026	349

Injection and production were processed and standardized to ensure consistency across all wells. The reporting period was converted into a datetime format, and records with invalid or missing dates were excluded. Only relevant variables were retained, including date and volumetric measurements (injection or production). All processed well-level datasets were then concatenated into unified injection and production datasets.

Vertical displacement measurements derived from InSAR were spatially intersected with the localized high-deformation zone polygons. For each acquisition date, deformation values were averaged across all points within each zone to generate zone-scale deformation time series. These time series were subsequently aggregated to a monthly temporal resolution to ensure consistency with the injection and production datasets.

Monthly injection and production data were aggregated by zone and merged using common temporal (date) and spatial (zone) identifiers. A monthly net fluid balance was then computed as the difference between injection and production.

To characterize long-term reservoir behaviour, cumulative injection, cumulative production, and cumulative net fluid balance were calculated as running sums for each zone after chronological sorting of the time series.

The resulting deformation and reservoir balance datasets were integrated to enable direct comparison between vertical surface displacement and subsurface fluid dynamics.

3. Results and Discussion

3.1 Ascending and Descending LOS velocities

The line-of-sight (LOS) velocities derived independently from ascending and descending Sentinel-1 radar imagery between November 2022 and October 2025 reveal a low-magnitude deformation field (< ± 2 cm/year) across the study area (Figure 4a & 4c).

Both viewing geometries consistently delineate a localized deformation pattern characteristic of oil-field activity, with a clearly defined subsidence–uplift pair within the central sector of the scene. The maximum LOS displacement rates, reaching approximately 1.5–1.7 cm/year, spatially coincide with the primary hydrocarbon production zones, suggesting a strong correlation between observed ground motion and fluid extraction operations.

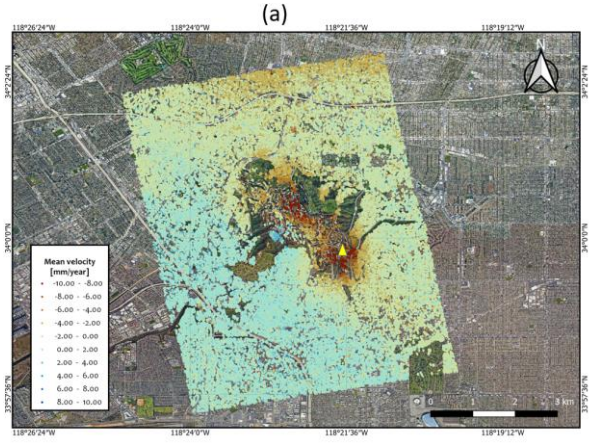

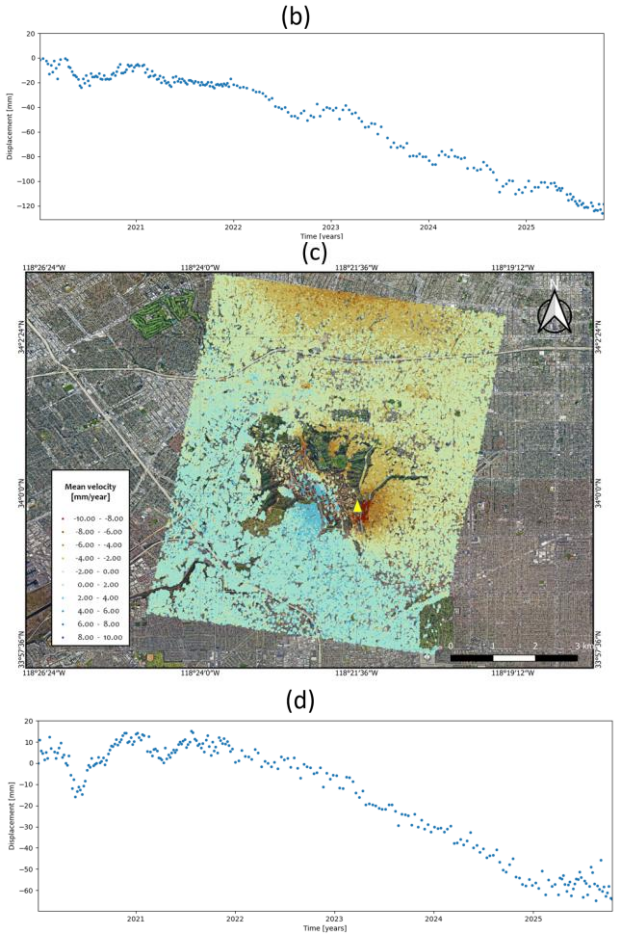

Figure 4. LOS velocity maps and displacement time series from Sentinel-1 data. (a) Ascending LOS velocity, (b) time series of the selected point (yellow triangle in a), (c) descending LOS velocity, and (d) corresponding time series of the selected point (yellow triangle in c).

Overall, the mean LOS deformation rates indicate a stable deformation regime, with most of the surrounding area exhibiting negligible motion (< 0.5 cm/year).

The trend in the timeseries displacement plot (Figure 4b and 4d) indicates a steady subsidence rate with minor seasonal fluctuations likely associated with periodic production cycles. The strong linear fit demonstrates the stability and coherence of the InSAR time-series over the five-year monitoring period.

The close agreement between the ascending and descending observations further supports the reliability of the measurements. The slight differences observed between the ascending and descending LOS velocity fields suggest the presence of minor horizontal components of ground motion. Therefore, the decomposition of InSAR LOS measurements into vertical and horizontal displacement components is essential to fully characterize the deformation mechanism and distinguish between vertical subsidence and lateral movement within the oilfield.

3.2 Vertical and Horizontal Deformation Results

This section presents the InSAR-derived vertical and horizontal deformation results generated from Sentinel-1 SAR data. The line-of-sight (LOS) decomposition provides enhanced insight into the deformation behaviour within the study area by separating vertical and horizontal motion components. These results were obtained through the joint decomposition of LOS deformation from both ascending and descending geometries.

This contribution has been peer-reviewed. The double-blind peer-review was conducted on the basis of the full paper.
https://doi.org/10.5194/isprs-annals-XI-3-2026-485-2026

Theoretically, a single ascending and descending acquisition pair is sufficient to perform such decomposition; however, the availability of multiple datasets from different look geometries enables a more robust and reliable estimation of displacement components (Fuhrmann & Garthwaite, 2019)
The vertical deformation field (Figure 5a) exhibits a maximum uplift rate of 0.8 cm/year and a maximum subsidence rate of −1.6 cm/year, indicating a dominant vertical motion pattern. These rates represent a low-magnitude but spatially coherent deformation signal over the five-year observation window. The deformation is localized within the oilfield, consistent with LOS observations and characteristic of reservoir compaction and elastic rebound processes.

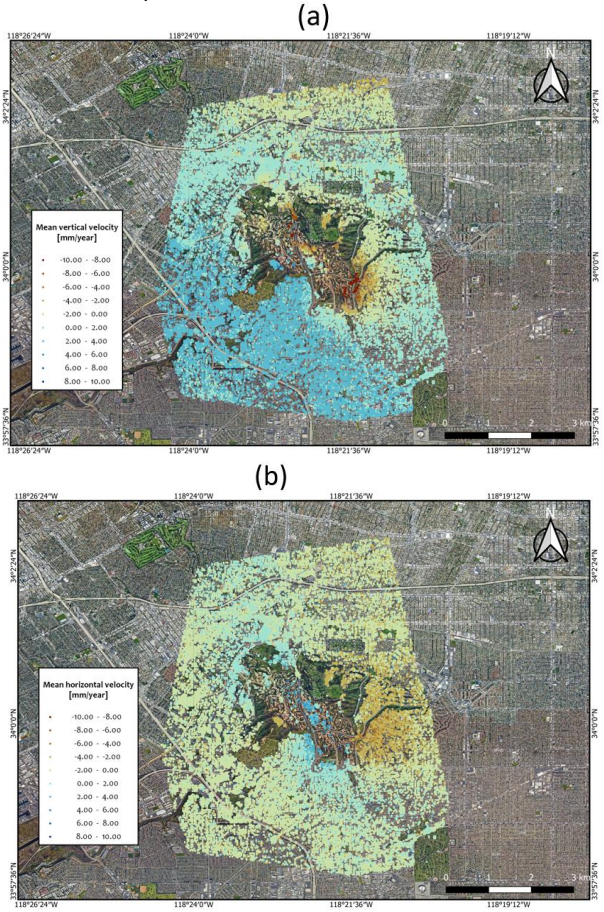

Figure 5. Vertical and horizontal deformation fields obtained from the decomposition of ascending and descending LOS velocities. (a) Mean vertical velocity and (b) mean horizontal (east–west) velocity, illustrating the spatial distribution of surface deformation.

In contrast, the horizontal deformation component (Figure 5b) displays relatively smaller magnitudes, with a maximum eastward displacement of 0.9 cm/year and a maximum westward displacement of −1.0 cm/year (−0.39 in/year). This indicates the presence of minor lateral motion, likely reflecting differential compaction or subtle structural influences at reservoir boundaries. The magnitude of the horizontal displacement is notably lower than the vertical component, confirming that deformation in this area is predominantly vertical.
The results are compared with those reported by (Walker, 2025), which assessed vertical deformation between 25th June 2023 and 1st July 2024, an uplift of 4.4 cm (1.75 in) and subsidence of −1.9 cm (−0.75 in) were recorded, the present results indicate a reduction in uplift and a slightly increased subsidence amplitude. The persistence of similar deformation zones but lower magnitudes suggests that the overall process remains active but slow.
When compared with the east–west displacement results from previous investigation - which reported 2.4 cm (0.96 in) eastward and −1.3 cm (−0.53 in) westward motion - the current analysis reveals a slight reduction in horizontal displacement magnitude. Similar directional pattern but smaller amplitudes indicate a progressive stabilization of both vertical and lateral deformation.

3.3 Data Aggregation

The localized high-deformation zones used in this study were delineated from the InSAR mean deformation velocity map shown in Figure 6. For each acquisition date, deformation values were spatially averaged across all InSAR points within each zone to derive a representative zone-scale deformation value. The resulting zone-level time series were subsequently aggregated to monthly mean values to match the temporal resolution of the injection and production datasets.
For visualization purposes, the well data time series were restricted to the period after 2000, as earlier records are characterized by prolonged intervals of negligible or missing injection data that do not contribute meaningfully to the analysis.

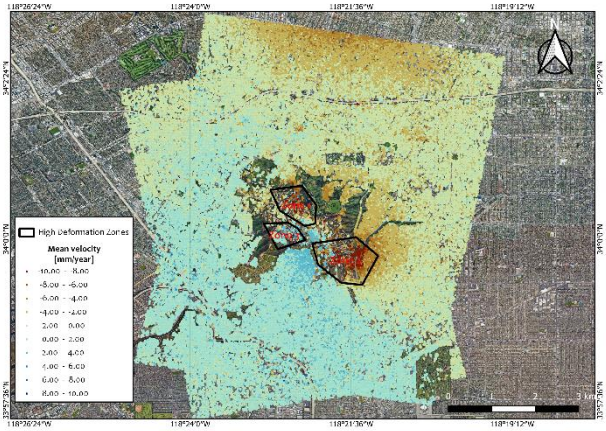

Figure 6. Spatial distribution of mean deformation velocity derived from InSAR data (ascending and descending), showing the delineation of localized high-deformation zones (outlined) within the study area. These zones define the spatial units used for subsequent analysis.

The results reveal distinct temporal patterns in injection activity across the study area (Figure 7), with significant variability both within and between zones. Periods of negligible injection are observed in the early portions of the record, followed by phases of sustained and, in some cases, intensified injection. Notably, zone 3 exhibits consistently higher injection volumes compared to the other zones, while zones 1 and 2 display more moderate and intermittent injection behaviour. These variations in injection intensity and timing provide an
initial indication of potential differences in reservoir pressurization, which may influence the observed surface deformation patterns.

This contribution has been peer-reviewed. The double-blind peer-review was conducted on the basis of the full paper.
https://doi.org/10.5194/isprs-annals-XI-3-2026-485-2026 | © Author(s) 2026. CC BY 4.0 License.

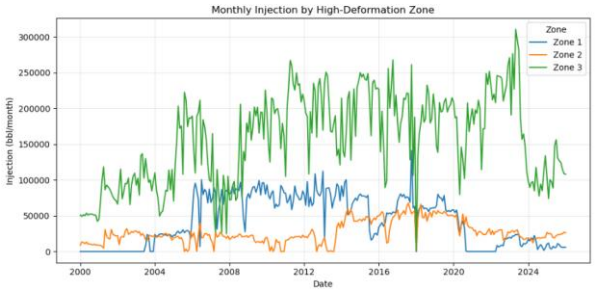

Figure 7. Monthly injection volumes aggregated by localized high-deformation zone.

Figure 8. Monthly production volumes aggregated by localized high-deformation zone.

Figure 8 shows the aggregated monthly production for the localized high-deformation zones. zone 2 exhibits the highest and most sustained production, while zones 1 and 3 display lower and more variable trends. These differences reflect variations in reservoir behaviour relevant to the observed surface deformation.

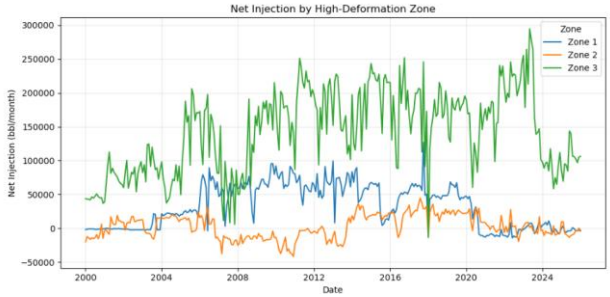

Figure 9. Monthly net fluid balance (injection minus production) aggregated by localized high-deformation zones.

Figure 9 shows the monthly net fluid balance for the localized high-deformation zones. zone 3 exhibits consistently positive values throughout the study period, indicating sustained fluid addition. In contrast, zone 1 shows moderate positive balance with intermittent variability, while zone 2 displays frequent transitions between positive and negative values, reflecting alternating periods of fluid injection and withdrawal.

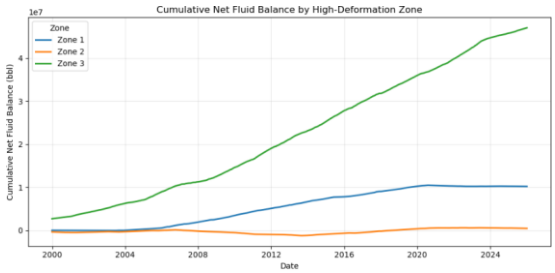

Figure 10. Cumulative net fluid balance aggregated by localized high-deformation zones.

In Figure 10 shows the cumulative net fluid balance for the localized high-deformation zones are visualized. zone 3 exhibits a pronounced and continuous increase, indicating sustained net fluid addition and progressive reservoir pressurization. zone 1 shows moderate cumulative growth, which stabilizes in the later period, while zone 2 remains near zero with minor fluctuations, reflecting limited net fluid accumulation. These differences highlight strong spatial variability in long-term reservoir storage conditions across the study area.

The sustained increase in cumulative net fluid balance observed in zone 3 provides strong evidence of long-term fluid accumulation and reservoir pressurization. This behaviour is consistent with the observed dominance of uplift in this zone, suggesting that fluid injection is a primary driver of surface deformation.

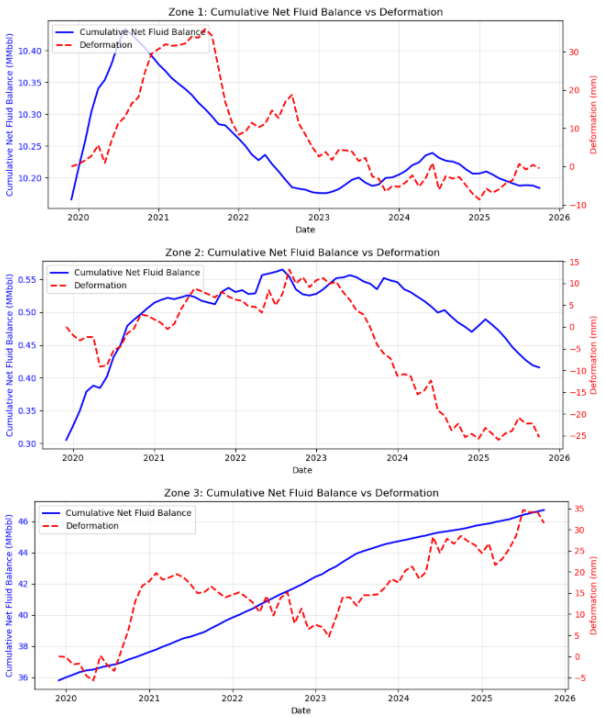

Figure 11. Comparison of vertical deformation (mm) and cumulative net fluid balance (MMbbl) for the localized high-deformation zones. Zones with sustained net fluid accumulation exhibit uplift, whereas zones characterized by declining fluid balance show subsidence

The integration of vertical InSAR-derived deformation with reservoir fluid balance reveals spatial variability in the relationship between subsurface processes and surface response across the identified high-deformation zones. The results (Figure 11) demonstrate that both the magnitude and temporal evolution of deformation are closely linked to the long-term balance between fluid injection and production, although the strength of this relationship varies between zones.

In zone 3, cumulative net fluid balance exhibits a sustained and monotonic increase, indicating continuous net fluid addition and progressive reservoir pressurization. This behaviour is consistently associated with positive vertical displacement (uplift), as shown in both the time-series comparison and correlation analysis ($r \approx 0.75$). The relatively stable correlation across time lags suggests a persistent and direct relationship between fluid accumulation and deformation, indicating that uplift in this zone is primarily driven by long-term increases in reservoir fluid storage.

This contribution has been peer-reviewed. The double-blind peer-review was conducted on the basis of the full paper.
https://doi.org/10.5194/isprs-annals-XI-3-2026-485-2026 | © Author(s) 2026. CC BY 4.0 License.

In zone 1, cumulative net fluid balance increases during the early period before stabilizing and slightly declining. The deformation signal reflects a transition from uplift to subsidence, broadly consistent with the evolution of the cumulative balance. The lag analysis indicates that the correlation between cumulative net fluid balance and deformation increases with time delay, reaching a maximum at approximately 5–6 months ($r \approx 0.88$). This suggests that deformation in zone 1 responds to reservoir processes with a measurable delay, likely reflecting time-dependent pressure diffusion or mechanical adjustment within the subsurface.

In contrast, zone 2 exhibits the highest magnitude of vertical deformation, characterized predominantly by subsidence, particularly during the later period of the time series. This behaviour corresponds with a decline in cumulative net fluid balance, indicating a transition toward net fluid withdrawal. The observed subsidence is therefore consistent with reservoir depletion and pressure reduction. However, the correlation between cumulative net fluid balance and deformation in zone 2 is comparatively weak ($r \approx 0.42$ at zero lag and decreasing with increasing lag), suggesting that the relationship between fluid balance and deformation is less direct than in the other zones.

The weaker coupling observed in zone 2 suggests that additional factors may influence the deformation in this area. These may include variations in reservoir properties (e.g., compressibility and permeability), structural controls such as faulting, or differences in the depth and spatial distribution of injection and production wells. Furthermore, as indicated in Table 1, the analysis is based on a limited subset of active wells, which may not fully represent the total fluid dynamics within the reservoir. Consequently, the observed relationship between deformation and fluid balance may be incomplete, and incorporating a more comprehensive set of wells could potentially alter the strength and interpretation of the correlation. While the overall subsidence trend remains consistent with decreasing fluid balance, the reduced correlation suggests that fluid withdrawal alone may not fully account for the observed deformation.

4. Conclusion

This study employed Sentinel-1 Interferometric Synthetic Aperture Radar (InSAR) time-series analysis to monitor ground deformation within the Inglewood oilfield. The analysis of ascending and descending datasets revealed a localized, low-magnitude deformation pattern dominated by vertical motion, with maximum uplift and subsidence rates of approximately +0.8 cm/yr and −1.6 cm/yr, respectively. Minor horizontal displacements of up to ±1.0 cm/yr indicate limited lateral strain associated with reservoir compaction and stress redistribution.

When compared with previous assessments, the results demonstrate a notable reduction in deformation magnitude, implying a gradual stabilization of reservoir pressure and more effective subsurface management. This study also demonstrates a clear relationship between reservoir fluid balance and vertical surface deformation within localized high-deformation zones. By integrating InSAR-derived vertical displacement with well-based injection and production data, the analysis shows that long-term fluid accumulation is associated with uplift, while net fluid withdrawal corresponds to subsidence.

Among the analyzed zones, zone 3 exhibits the strongest and most consistent coupling between cumulative net fluid balance and deformation, indicating that reservoir pressurization is a dominant control on uplift in this area. zone 1 shows a delayed but significant response to fluid balance changes, highlighting the importance of temporal lag in deformation processes. In contrast, zone 2, despite exhibiting the highest magnitude of subsidence, shows weaker correlation with fluid balance, suggesting that additional geological or operational factors, as well as the influence of other wells not included in this study may influence deformation behaviour.

The study confirms the reliability and sensitivity of InSAR for detecting subtle surface movements within oilfields. These findings highlight the importance of continued spaceborne monitoring for evaluating reservoir behaviour, mitigating surface stability risks, and guiding sustainable production practices.

5. Limitation of Studies and Future work

It is important to note that the present analysis is based on a limited subset of injection and production wells selected within localized high-deformation zones. As such, the derived relationships between reservoir fluid balance and surface deformation may not fully represent the behaviour of the entire study area. A more comprehensive assessment incorporating all active injection and production wells would provide a more robust characterization of reservoir-wide fluid dynamics and their influence on deformation patterns. In addition, future work will extend the InSAR time series to a longer temporal range to better capture long-term deformation trends and improve the robustness of the observed relationships between reservoir processes and surface response.

The integration of InSAR observations with geophysical and inversion modeling continues to advance our understanding of subsurface deformation processes in hydrocarbon-producing regions. Elastic and poroelastic inversion models, as demonstrated by Lee et al. (2023), effectively link observed surface deformation with underlying mechanisms such as reservoir compaction, inflation, and aseismic fault slip. These approaches provide a quantitative basis for interpreting complex deformation fields influenced by fluid extraction and injection.

Future research will also aim to derive the three-dimensional (3D) surface deformation field across the Inglewood oilfield. The east–west displacement component has already been obtained, and the north–south component will be estimated by assuming a physical relationship between horizontal and vertical displacement, following the approach of Tang et al. (2024) The reconstructed 3D deformation field will be analysed using the Geertsma nucleus-of-strain model (Geertsma, 1973) to quantify reservoir compaction, assess stress redistribution, and delineate the lateral extent of deformation associated with hydrocarbon production. Such integration of InSAR-derived 3D deformation with geomechanical modeling is expected to provide improved insight into subsurface processes and support more effective monitoring and management of the Inglewood oilfield.

6. References

Berardino, P., Fornaro, G., Lanari, R., & Sansosti, E. (2003). A new algorithm for surface deformation monitoring based on small baseline differential SAR interferograms. *IEEE Transactions on Geoscience and Remote Sensing*, *40*(11), 2375–2383.

Bioucas-Dias, J. M., & Valadao, G. (2007). Phase Unwrapping via Graph Cuts. *IEEE Transactions on Image Processing*, *16*(3), 698–709. https://doi.org/10.1109/TIP.2006.888351

Boykov, Y., & Kolmogorov, V. (2004). An experimental comparison of min-cut/max- flow algorithms for energy minimization in vision. *IEEE Transactions on Pattern Analysis and Machine Intelligence*, *26*(9), 1124–1137. https://doi.org/10.1109/TPAMI.2004.60

Castle, R. O., & Yerkes, R. F. (1976). *Recent surface movements in the Baldwin Hills, Los Angeles County, California*. US Govt. Print. Off.,.

Chilingar, G. V, & Endres, B. (2005). Environmental hazards posed by the Los Angeles Basin urban oilfields: an historical perspective of lessons learned. *Environmental Geology*, *47*(2), 302–317. https://doi.org/10.1007/s00254-004-1159-0

Elliott, J. R., Walters, R. J., & Wright, T. J. (2016). The role of space-based observation in understanding and responding to active tectonics and earthquakes. *Nature Communications*, *7*(1), 13844. https://doi.org/10.1038/ncomms13844

Fielding, E. J., Blom, R. G., & Goldstein, R. M. (1998). Rapid subsidence over oil fields measured by SAR interferometry. *Geophysical Research Letters*, *25*(17), 3215–3218.

Fokker, Peter. A., van Leijen, Freek. J., Orlic, B., van der Marel, H., & Hanssen, R. F. (2018). Subsidence in the Dutch Wadden Sea. *Netherlands Journal of Geosciences*, *97*, 129–181. https://doi.org/10.1017/njg.2018.9

Fuhrmann, T., & Garthwaite, M. C. (2019). Resolving three-dimensional surface motion with InSAR: Constraints from multi-geometry data fusion. *Remote Sensing*, *11*(3), 241.

Geertsma, J. (1973). Land subsidence above compacting oil and gas reservoirs. *JPT, Journal of Petroleum Technology*, *25*, 734 – 744. https://doi.org/10.2118/3730-PA

Grebby, S., Orynbassarova, E., Sowter, A., Gee, D., & Athab, A. (2019). Delineating ground deformation over the Tengiz oil field, Kazakhstan, using the Intermittent SBAS (ISBAS) DInSAR algorithm. *International Journal of Applied Earth Observation and Geoinformation*, *81*, 37–46.

Inglewood oil Field. (2025). *History of Inglewood Oil Field*. https://inglewoodoilfield.com/

Karanam, V., & Lu, Z. (2023). Hydrocarbon production induced land deformation over Permian Basin; analysis using persistent scatterer interferometry and numerical modeling. *International Journal of Applied Earth Observation and Geoinformation*, *122*, 103424. https://doi.org/10.1016/J.JAG.2023.103424

Ketelaar, V. B. H. (2009). *Satellite radar interferometry: Subsidence monitoring techniques*. Springer.

Lee, H. P., Staniewicz, S., Chen, J., Hennings, P., & Olson, J. E. (2023). Subsurface deformation monitoring with InSAR and elastic inversion modeling in west Texas. *Geoenergy Science and Engineering*, *231*, 212299. https://doi.org/10.1016/J.GEOEN.2023.212299

Liu, Y., Huang, H., Liu, Y., & Bi, H. (2016). Linking land subsidence over the Yellow River delta, China, to hydrocarbon exploitation using multi-temporal InSAR. *Natural Hazards*, *84*(1), 271–291.

Lu Zhong and Dzurisin, D. (2014). InSAR Imaging of Aleutian Volcanoes. In *InSAR Imaging of Aleutian Volcanoes: Monitoring a Volcanic Arc from Space* (pp. 87–345). Springer Berlin Heidelberg. https://doi.org/10.1007/978-3-642-00348-6_6

Motagh, M., Shamshiri, R., Haghshenas Haghighi, M., Wetzel, H. U., Akbari, B., Nahavandchi, H., Roessner, S., & Arabi, S. (2017). Quantifying groundwater exploitation induced subsidence in the Rafsanjan plain, southeastern Iran, using InSAR time-series and in situ measurements. *Engineering Geology*, *218*, 134–151. https://doi.org/10.1016/J.ENGGEO.2017.01.011

Piter, A., Haghshenas Haghighi, M., & Motagh, M. (2025). *SARvey-survey with SAR.*

Ringrose, P. S., Mathieson, A. S., Wright, I. W., Selama, F., Hansen, O., Bissell, R., Saoula, N., & Midgley, J. (2013). The In Salah CO2 Storage Project: Lessons Learned and Knowledge Transfer. *Energy Procedia*, *37*, 6226–6236. https://doi.org/https://doi.org/10.1016/j.egypro.2013.06.551

Rocca, F., Rucci, A., & Bohane, A. (2013). Advanced InSAR interferometry for reservoir monitoring. *First Break*, *31*(5), 77–85. https://www.scopus.com/inward/record.uri?eid=2-s2.0-84877664362&partnerID=40&md5=467629a89f05c616cfe99599fa62376a

Samsonov, S., & d’Oreye, N. (2012). Multidimensional time-series analysis of ground deformation from multiple InSAR data sets applied to Virunga Volcanic Province. *Geophysical Journal International*, *191*(3), 1095–1108.

Shi, J., Xu, B., Chen, Q., Hu, M., & Zeng, Y. (2022). Monitoring and analysing long-term vertical time-series deformation due to oil and gas extraction using multi-track SAR dataset: A study on lost hills oilfield. *International Journal of Applied Earth Observation and Geoinformation*, *107*, 102679. https://doi.org/10.1016/J.JAG.2022.102679

Staniewicz, S., Chen, J., Lee, H., Olson, J., Savvaidis, A., Reedy, R., Breton, C., Rathje, E., & Hennings, P. (2020). InSAR Reveals Complex Surface Deformation Patterns Over an 80,000 km2 Oil-Producing Region in the Permian Basin. *Geophysical Research Letters*, *47*(21). https://doi.org/10.1029/2020GL090151

Tamburini, A., Bianchi, M., Giannico, C., & Novali, F. (2010). Retrieving surface deformation by PSInSAR™ technology: A powerful tool in reservoir monitoring. *International Journal of Greenhouse Gas Control*, *4*(6), 928–937. https://doi.org/https://doi.org/10.1016/j.ijggc.2009.12.009

Tang, W., Gong, Z., Sun, X., Liu, Y., Motagh, M., Li, Z., Li, J., Malinowska, A., Jiang, J., Wei, L., Zhang, X., Wei, X., Li, H., & Geng, X. (2024). Three-dimensional surface deformation from multi-track InSAR and oil reservoir characterization: A case study in the Liaohe Oilfield, northeast China. *International Journal of Rock Mechanics and Mining Sciences*, *174*, 105637. https://doi.org/10.1016/J.IJRMMS.2024.105637

Walker, T. (2025). *Baldwin Hills Community Standards District Inglewood Oil Field Surface Monitoring Program Evaluation of 2023-24 Survey and Production Data*.

Wegnüller, U., Werner, C., Strozzi, T., Wiesmann, A., Frey, O., & Santoro, M. (2016). Sentinel-1 Support in the GAMMA Software. *Procedia Computer Science*, *100*, 1305–1312. https://doi.org/10.1016/J.PROCS.2016.09.246

Wright, T. (1987). *The Inglewood oil field*.

Xu, L., Yang, Y., Ju, X., & Yang, J. (2023). Influence of geological factors on surface deformation due to hydrocarbon exploitation using time-series InSAR: A case study of Karamay Oilfield, China. *Frontiers in Earth Science*, *10*, 983155.

Yang, C., Zhang, D., Zhao, C., Han, B., Sun, R., Du, J., & Chen, L. (2019). Ground deformation revealed by Sentinel-1 MSBAS-InSAR time-series over Karamay Oilfield, China. *Remote Sensing*, *11*(17), 2027.

Zhao, F., & Mallorqui, J. (2019). A Temporal Phase Coherence Estimation Algorithm and Its Application on DInSAR Pixel Selection. *IEEE Transactions on Geoscience and Remote Sensing*, *PP*. https://doi.org/10.1109/TGRS.2019.2920536